Research Square

Preprints are preliminary reports that have not undergone peer review.
They should not be considered conclusive, used to inform clinical practice,
or referenced by the media as validated information.

A chamber-height-defined microfluidic platform for comparative screening of microalgal phenotypic and bioproduct-associated Raman responses

Junyi Yao
University of Virginia
Jee Young Kim
Ajou University
Heewoong Ko
Korea University
Ammasi Periasamy
University of Virginia
Jaewon Park
netjay@korea.ac.kr
Korea University

Research Article

Keywords: Mechanical confinement, Microfluidics, Microalgae, Single-cell Raman spectroscopy, Bioproduct screening

Posted Date: November 25th, 2026

DOI: https://doi.org/10.21203/rs.3.rs-11753349/v1

License: This work is licensed under a Creative Commons Attribution 4.0 International License.
Read Full License

Additional Declarations: No competing interests reported.

A chamber-height-defined microfluidic platform for comparative screening of microalgal phenotypic and bioproduct-associated Raman responses

Junyi Yao[a], Jee Young Kim[b], Heewoong Ko[c], Ammasi Periasamy[d], and Jaewon Park[c, e *]

[a] Department of Chemistry, University of Virginia, Charlottesville, USA

[b] Department of Environmental and Safety Engineering, Ajou University, Suwon, Korea

[c] Department of Control and Instrumentation Engineering, Korea University, Sejong, Korea

[d] Department of Biology and Keck Center for Cellular Imaging, University of Virginia, Charlottesville, USA

[e] Department of Electro-Mechanical Systems Engineering, Korea University, Sejong, Korea

* Correspondence to:

Jaewon Park

Rm. 409, Science and Technology Bldg. 1, Korea University, Sejong 30019, Republic of Korea

E-mail: netjay@korea.ac.kr, Tel: +82-44-860-1447; Fax: +82-44-860-1587

Abstract

Background Physical confinement provides a potential non-chemical strategy for modulating microalgal phenotypes and bioproduct-associated responses, but comparative on-chip platforms for different species remain limited.

Results Here, we developed a star-shaped microfluidic platform that applies chamber-height-defined confinement to microalgal cells and enables multiple chamber-height conditions to be compared within a single chip for each species. Three microalgal species with distinct cell sizes and morphologies, *C. reinhardtii*, *H. pluvialis*, and *E. gracilis*, were examined using image-based growth and morphology/phenotype analysis together with label-free single-cell Raman spectroscopy. The platform revealed species- and readout-dependent responses to confinement. In *C. reinhardtii*, cells progressively occupied the tested chambers, while projected cell-size distributions and lipid-associated Raman signals varied with chamber height, with the two lipid-associated bands reaching their highest mean intensities at different heights. In *H. pluvialis*, the 15 μm chamber showed the highest mean red-cyst area fraction and astaxanthin-associated Raman intensities among the tested on-chip chamber-height conditions. In *E. gracilis*, shallower chambers were associated with a more compact morphology, while single-cell Raman measurements showed lower carotenoid-associated signals in the cells examined under confinement.

Conclusions The platform provides a practical framework for comparative microalgal screening by linking chamber-height conditions with species-specific phenotypic and bioproduct-associated Raman responses.

Keywords

Mechanical confinement; Microfluidics; Microalgae; Single-cell Raman spectroscopy; Bioproduct screening

Background

Microalgae are versatile biological sources capable of producing a wide range of high-value compounds, including lipids, carotenoids, and polysaccharides, with growing applications in medicine, pharmaceuticals, biofuels, nutraceuticals, cosmetics, and other industrial sectors [1, 2]. *Chlamydomonas reinhardtii* (*C. reinhardtii*), *Haematococcus pluvialis* (*H. pluvialis*), and *Euglena gracilis* (*E. gracilis*) are representative microalgal species with distinct bioproduct profiles and physiological characteristics [3, 4, 5]. *C. reinhardtii* can accumulate lipids suitable for biofuel production under specific growth conditions and is widely used as a model organism for studying algal lipid metabolism [3]. *H. pluvialis* is considered one of the richest natural sources of astaxanthin (3,3′-dihydroxy-β-carotene-4,4′-dione), a bright red ketocarotenoid with strong antioxidant activity and broad commercial value in nutraceuticals, feed, cosmetics, and pharmaceutical applications [4]. *E. gracilis* is a promising bioproduction host because it can produce diverse intracellular products, including paramylon, lipids, carotenoids, and vitamins [5, 6]. Paramylon is a β-1,3-glucan polysaccharide with immunomodulatory properties, and dietary paramylon has shown preventive effects against preneoplastic colonic lesions in mice [5, 7]. Sulfated derivatives of paramylon, rather than native paramylon, have also shown *in vitro* anti-HIV activity [8]. Lipids and β-carotene from *E. gracilis* are additionally of interest for biodiesel production and antioxidant applications [9, 10].

Despite the high potential of algae-derived products, efficient and controllable production of microalgal biomass and intracellular bioproducts remains a major challenge for commercial implementation [1, 2]. Microalgae commonly overproduce target bioproducts under stress conditions such as nitrogen limitation, iron starvation, high-light exposure, and other conventional cultivation stresses [3, 4, 11, 12]. These approaches rely on sustained environmental stress that can require days to weeks for the metabolic response to develop [11, 12]. During this period, prolonged nutrient deficiency can reduce growth or viability, while bulk cultivation can generate heterogeneous local conditions across the cell population [11, 13, 14]. These factors reduce experimental controllability and make it difficult to attribute bioproduct accumulation to a specific stimulus [11, 13]. Mechanical stress offers a controllable alternative because it can be applied without changing the culture-medium composition, allowing nutrient supply to be maintained during cultivation. Mechanical stimulation can therefore be separated from nutritional stress, enabling direct investigation of how physical confinement affects cellular growth, morphology, and bioproduct-associated responses [14, 15, 16].

Microfluidic BioMEMS platforms provide stable cell-scale environments for controlling and monitoring cell responses. Their small culture volumes allow real-time observation and precise control of local conditions, making them useful for screening algal growth and stress responses [13]. In *C. reinhardtii*, direct membrane distortion has been shown to alter the physiology and cell-cycle behavior [15]. Cho and Shin reported that compression enhanced lipid productivity through mechanotransduction, while porous microbeads supplied nutrients and reduced cell death [14]. Our previous work showed that mechanical confinement enhanced astaxanthin accumulation in *H. pluvialis*, with the 15 μm chamber producing approximately ninefold greater accumulation than the no-stress condition after 7 days [16]. However, these studies used devices designed for

individual species. To our knowledge, a comparable chamber-height-defined mechanical-confinement study has not been reported for *E. gracilis*, although confinement is known to trigger marked behavioral and morphological changes in this species [17]. A common device format is therefore needed to compare chamber-height-dependent responses across microalgal species with different cell sizes and morphologies [14, 16, 17].

In this study, we developed a star-shaped microfluidic platform that applies chamber-height-defined confinement to microalgal cells and enables species-dependent responses to be compared within a common device format. The platform was applied to three microalgal species with distinct cell sizes and morphologies, *C. reinhardtii*, *H. pluvialis*, and *E. gracilis*, to investigate how chamber-height-defined confinement influences growth, morphology or phenotype, and bioproduct-associated responses, using image-based analysis and label-free single-cell Raman spectroscopy. By integrating multiple chamber-height conditions within a single chip for each species, this approach provides a framework for comparative evaluation of microalgal responses under defined physical environments.

Material and Methods

Microfluidic device design and confinement conditions

Chamber-height-defined confinement was applied to cells by limiting the height of the cell culture chambers. The star-shaped microfluidic platform comprised five radial branches, each assigned to one chamber-height condition (Figure 1). Each branch contained four culture chambers of identical height, serving as replicate chambers for that height condition. In total, the device contained 20 culture chambers, each with a nominal footprint of 200 × 100 μm and one of five chamber heights: 3, 5, 10, 15, and 40 μm. The five chamber heights were designed to accommodate the varying cell

sizes and morphologies of the three species: *C. reinhardtii* cells are approximately 8–12 μm in diameter [18], *H. pluvialis* cells in the motile vegetative stage typically range from 15–20 μm [16, 19], and *E. gracilis* cells are elongated, deformable, and responsive to geometric confinement [17]. The mean loading-day dimensions used for the compression-ratio calculations were approximately 11.5 μm for *C. reinhardtii*, 19.8 μm for *H. pluvialis*, and 12.6 μm for the cell width (minor axis) of *E. gracilis* (Table 1). Selection of chamber heights smaller than or comparable to the relevant cell dimensions enabled chamber-height-defined vertical confinement to be applied to each species.

To quantify the degree of initial vertical compression, we defined the initial compression ratio as max [(cell dimension − chamber height) / cell dimension × 100%, 0], calculated using cell

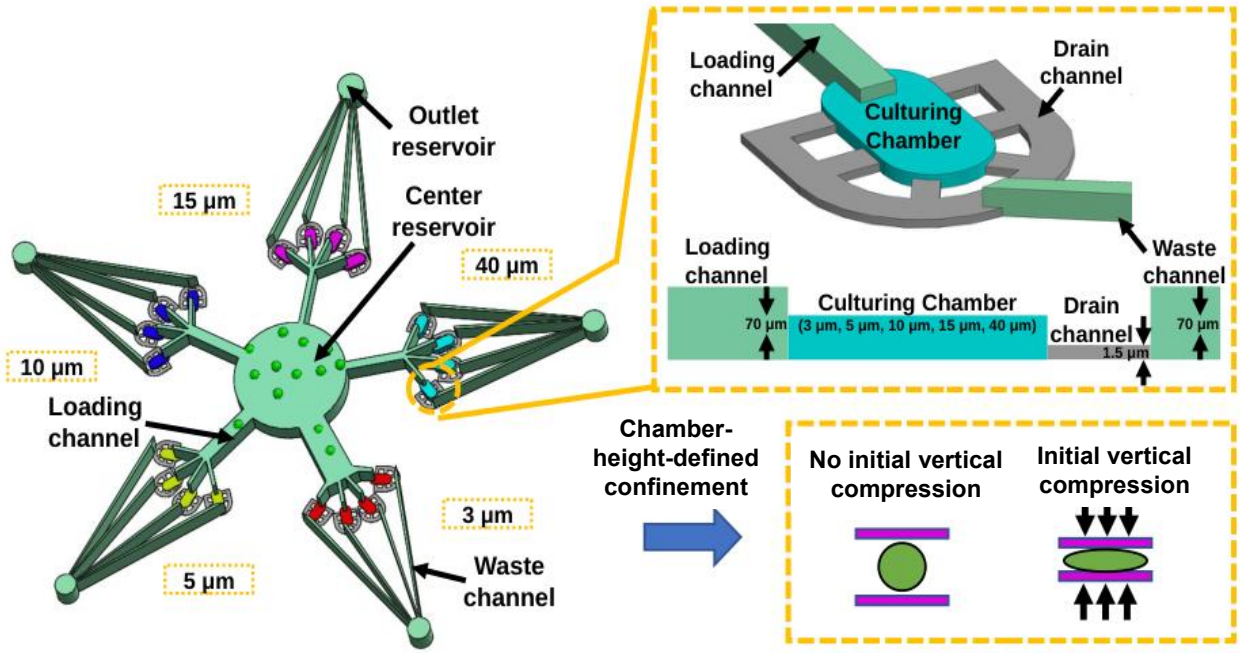

Figure 1. Star-shaped microfluidic platform for chamber-height-defined confinement. Five radial branches contain four culture chambers each at 3, 5, 10, 15, or 40 μm. Each culture chamber connects directly to a loading channel and to a waste channel through a 1.5 μm-high drain channel; the loading and waste channels are 70 μm high. Insets illustrate the chamber geometry and initial vertical confinement.

diameter for *C. reinhardtii* and *H. pluvialis* and cell width for *E. gracilis* at the time of loading (Table 1). Values that would be negative because the chamber was taller than the measured cell dimension were reported as 0%, indicating no initial vertical compression. For example, the 5 µm chamber for *C. reinhardtii* corresponds to an initial compression ratio of approximately 57%, while the 15 µm chamber for *H. pluvialis* provides an initial compression ratio of approximately 24%. Notably, for species that undergo substantial morphological changes during cultivation, such as the encystment of *H. pluvialis*, the extent of geometric restriction may change as cells enlarge within fixed-height chambers. The initial compression ratios for all species and chamber-height combinations are summarized in Table 1.

Table 1. Initial chamber-height-defined confinement of each microalgal species. Initial compression ratio = max [(cell dimension − chamber height) / cell dimension × 100%, 0], using cell diameter for *C. reinhardtii* and *H. pluvialis* and cell width (minor axis) for *E. gracilis*. For *E. gracilis*, values in parentheses are the nominal geometric restriction index based on major axis, which reflects out-of-plane restriction rather than axial compression. The tallest tested chamber is the designated on-chip control. "—" indicates untested chamber heights.

Chamber height (µm)	*C. reinhardtii*	*H. pluvialis*	*E. gracilis*
Reference dimension (µm)	Diameter 11.5	Diameter 19.8	Minor axis 12.6; major axis 31.6
3	74%	—	—
5	57%	—	—
10	13%	50%	20% (68%)
15	0% **(control)**	24%	0% (53%)
40	—	0% **(control)**	0% **(control)**

E. gracilis required an additional descriptor because its cell body is strongly anisotropic. At loading, the mean major and minor axes of *E. gracilis* were approximately 31.6 ± 10.3 µm and 12.6 ± 3.5 µm, respectively (mean ± SD; n = 139 cells pooled across chamber heights on the loading day). The mean loading-day major axis therefore exceeds every chamber height except 40

μm, so vertical confinement restricts the orientation of the cell body and the large-amplitude shape excursions associated with metaboly before it compresses the cell cross-section. We consequently described *E. gracilis* confinement using two complementary descriptors: the width-based initial compression ratio defined above, and a nominal geometric restriction index defined as max [(major axis − chamber height) / major axis × 100%, 0]. The 10, 15, and 40 μm chambers correspond to geometric restriction indices of approximately 68%, 53%, and 0%, and to width-based compression ratios of approximately 20%, 0%, and 0%, respectively. The geometric restriction index is not a measure of axial compression, because an elongated cell can lie with its long axis in the horizontal plane of the chamber; it indexes out-of-plane restriction. The 40 μm chamber exceeded both mean loading-day cell dimensions and was designated as the *E. gracilis* on-chip control.

Each culture chamber connected directly to a loading channel and communicated with a 70 μm-high waste channel through a shallow 1.5 μm-high drain channel (Figure 1, inset). The shallow drain channel restricted cell passage during reservoir-level-driven medium exchange. The tallest tested chamber was designated as the species-specific control: 15 μm for *C. reinhardtii* and 40 μm for *H. pluvialis* and *E. gracilis*. Accordingly, *C. reinhardtii* was tested at 3, 5, 10, and 15 μm, and *H. pluvialis* and *E. gracilis* were tested at 10, 15, and 40 μm.

Device fabrication

The master molds were fabricated by conventional photolithography using SU-8™ negative photoresist (MicroChem Corp.) on a 3-inch silicon wafer (Figure S1). The structure consisted of seven sequentially patterned layers: a shallow drain-channel layer (1.5 μm), five culture-chamber layers of different heights (3, 5, 10, 15, and 40 μm), and a loading-channel layer (70 μm). Each layer was soft-baked at 60 °C and 95 °C, exposed to UV light using a mask aligner (MA6, SUSS

MicroTec AG, Germany), and post-exposure-baked at 60 °C and 95 °C. Successive layers were registered to the preceding layers using alignment marks patterned in the first lithography step. The pattern was then developed using SU-8™ developer (Sigma-Aldrich, St. Louis, MO, USA). This process was repeated for all seven layers to complete the master mold. The thickness of the SU-8™ features was measured using a surface profiler (D-120, KLA-Tencor), and the measured layer thicknesses were within the tolerance required for the chamber-height assignments used throughout this study.

The polydimethylsiloxane (PDMS) microfluidic platform was fabricated using standard PDMS soft-lithography (10:1 base-to-curing-agent ratio, Sylgard® 184, Dow Corning). First, the SU-8 master mold was treated with trichloro(1H,1H,2H,2H-tridecafluoro-n-octyl)silane (Tokyo Chemical Industry Co.) for 15 minutes. PDMS was then poured onto the mold and cured in an oven at 80 °C for 2 hours. The cured PDMS was peeled off, and center and outlet reservoir holes were punched using a biopsy punch (1.5 mm, Miltex, Plainsboro, NJ, USA). Finally, the PDMS device was irreversibly bonded to a cleaned glass substrate (76.2 × 25.4 mm^2, Sail Brand Co., China) by oxygen-plasma treatment (PDC-002, Harrick Plasma). The assembled platform was immersed in deionized (DI) water and exposed to UV light inside a biosafety cabinet for at least 40 min for sterilization prior to use.

Microalgal strains and pre-culture conditions

The unicellular microalgae *C. reinhardtii* CC-406 (cw15 mt^-), *H. pluvialis* (UTEX 2505), and *E. gracilis* strain Z (Klebs; CCALA 349) were selected as model organisms to demonstrate the functionality of the developed microfluidic system. These three species have distinct cell sizes and morphologies and were therefore used to evaluate the applicability of the platform to different

176 microalgal cell types. Cell concentrations were determined using a hemacytometer prior to
177 loading.

178 *C. reinhardtii* CC-406, a cell-wall-deficient (cw15) mutant [20], was obtained from the
179 Chlamydomonas Resource Center at the University of Minnesota (USA). Cells were cultured in
180 250 mL Erlenmeyer flasks containing 150 mL of Tris-acetate-phosphate (TAP) medium (Table
181 S1), a standard medium widely used for *C. reinhardtii* cultivation [18, 21], under continuous white
182 fluorescent illumination at 50 μmol photons m^{-2} s^{-1} and 23 ± 1 °C. Light intensity was measured
183 using a quantum sensor (MQ200, Apogee Instruments, USA), and aeration was provided at 1 vvm
184 of filtered air through sterilized syringe filters (0.22 μm, Millipore, USA). Cells were harvested on
185 Day 2 after transfer to fresh medium and diluted to 4×10^5 cells/mL for loading.

186 *H. pluvialis* UTEX 2505 was obtained from the Culture Collection of Algae at the
187 University of Texas at Austin (USA). Stock cultures were maintained predominantly in the
188 nonmotile aplanospore stage in 250 mL round-bottom flasks containing 150 mL of optimal
189 *Haematococcus* medium (OHM) (Table S2), prepared according to Fábregas *et al.* [22], under 50
190 μmol photons m^{-2} s^{-1} white fluorescent illumination at 23 ± 1 °C with aeration at 1 vvm through
191 0.22 μm sterilized syringe filters. As a reference for the morphological changes observed on-chip,
192 *H. pluvialis* is known to exist in multiple life-cycle stages, including motile flagellated vegetative
193 cells (15-20 μm), nonmotile palmelloid cells, and red aplanospores [16, 23]. Before loading into
194 the star-shaped culture device, the cell suspension was passed through the micropillar-array sorting
195 section of our previously reported microfluidic platform [16]. The micropillar array selectively
196 collected motile flagellated early-vegetative cells (approximately 15-20 μm) while excluding
197 nonmotile cyst-stage cells. The selected vegetative-cell fraction was adjusted to 4×10^6 cells/mL
198 and introduced into the present device.

E. gracilis strain Z (Klebs; CCALA 349) was obtained from the Culture Collection of Autotrophic Organisms at the Institute of Botany of the Czech Academy of Sciences. *E. gracilis* is metabolically versatile and can grow under photosynthetic, mixotrophic, or heterotrophic conditions [5, 6, 24, 25, 26]; in this study, cells were cultured heterotrophically in the dark to minimize light-induced metabolic effects during the chamber-height-defined confinement experiments. A colony from the agar stock was inoculated into a 50 mL Erlenmeyer flask containing 20 mL of modified Hutner medium [27] (Table S3) and cultivated in darkness at 25 ± 1 °C with orbital shaking at 150 rpm for 5 days. The first liquid culture was then transferred at 7.5% (v/v) into 100 mL of fresh Hutner medium in a 250 mL flask and cultivated for 48 h under the same conditions. Day 2 therefore refers to the second day after transfer into fresh medium. Young, actively growing early-exponential-phase cells were harvested at this time and diluted with Hutner medium to 5×10^4 cells/mL for loading.

Cell loading and on-chip cultivation

Cells were loaded into the center reservoir of the device and allowed to flow into the culture chambers of different heights. The time of loading was defined as the start of on-chip cultivation (loading day). The culture medium was replenished once per day by removing the spent medium from the outlet reservoirs and adding fresh medium to the center reservoir. The resulting difference in liquid level drove transient gravity-driven medium exchange until the liquid levels equilibrated. No continuous perfusion was applied. The species-specific medium used for pre-culture (TAP for *C. reinhardtii*, OHM for *H. pluvialis*, and Hutner medium for *E. gracilis*) was used for the daily replacement.

On-chip temperature and illumination conditions matched those of the respective pre-cultures. *C. reinhardtii* and *H. pluvialis* were maintained under 50 µmol photons m^{-2} s^{-1} white

fluorescent illumination at 23 ± 1 °C, whereas *E. gracilis* was cultured heterotrophically in the dark at 25 ± 1 °C, except during brief periods of optical imaging. *C. reinhardtii* was cultivated for 4 days, and *H. pluvialis* and *E. gracilis* were cultivated for 6 days. Each species was run on independently fabricated devices operated in parallel under its respective culture conditions, with four culture chambers per tested chamber height on each device. For the cultivation readouts in Figure 2, three devices were analyzed for *C. reinhardtii* and *H. pluvialis* and two for *E. gracilis*. For *H. pluvialis*, the numbers of identifiable chambers were 9, 8, and 12 for the 10, 15, and 40 μm conditions, respectively.

Microscopic imaging and cell growth/morphology analysis

Cell growth and morphological changes under chamber-height-defined confinement were monitored from microscopic images acquired daily throughout the cultivation period. Fluorescence and phase-contrast images were obtained using an inverted optical microscope (Observer.Z1, Carl Zeiss) equipped with a digital camera (Axiocam 503 color, Carl Zeiss) and analyzed using Fiji (ImageJ 1.54, National Institutes of Health, Bethesda, MD, USA) [28]. After scale-bar calibration, species-specific parameters were quantified using the Count, Major-axis, Minor-axis, and Area functions in Fiji. For *H. pluvialis* and *E. gracilis*, cell counts were normalized to the corresponding loading-day value.

For *C. reinhardtii*, chamber occupancy was calculated in Python from pre-existing binary chlorophyll-fluorescence TIFF masks within an image-defined chamber region of interest (ROI). During occupancy calculation, pixels with nonzero values in the supplied binary masks were classified as fluorescence-positive; no additional intensity threshold or background subtraction was applied at this stage. The chamber boundary was represented by a fitted ellipse, with the ROI reduced to 92% of the fitted ellipse diameters to exclude wall pixels. The ROI was partitioned into

64 × 64-pixel tiles. A tile was included when at least 25% of its nominal area lay inside the ROI, and was classified as occupied when at least 0.5% of its ROI pixels were fluorescence-positive. Raw spatial occupancy was defined as the number of occupied tiles divided by the number of analyzable tiles, multiplied by 100%. For each chamber height, raw chamber occupancies were averaged within each device and then across the three devices; the relative time course in Figure 2A was obtained by dividing each height-specific mean by its corresponding Day 4 mean and multiplying by 100%. The projected (two-dimensional) diameter of *C. reinhardtii* cells was measured in Fiji and is reported as mean ± standard deviation (SD), with cumulative distributions constructed from individual-cell measurements.

For *E. gracilis*, cell number and the major and minor axes were measured. Cell morphology was expressed as a shape index defined as minor axis / major axis; values closer to 1 indicate a more rounded cell shape. Individual-cell shape indices were averaged within each chamber, and chamber means were plotted.

For *H. pluvialis*, total projected cell area and red-pigmented area were measured from color micrographs using Fiji (ImageJ). When more than one red-pigmented region was recorded for a cell, the corresponding areas were summed. The red-cyst area fraction for each cell was calculated as the total red-pigmented area divided by the corresponding total projected cell area; cells with no detectable red-pigmented regions were assigned a fraction of zero. Cell-level fractions were first averaged within each identifiable culture chamber. For each chamber height and day, the value plotted in Figure 4B was the unweighted arithmetic mean of the available chamber means (two or three chambers per condition and time point), with error bars representing the SEM of those chamber means.

Raman spectroscopy and bioproduct-associated signal analysis

Bioproduct-associated Raman signals were measured using a confocal Raman microscope (LabRAM HR Evolution, Horiba) equipped with a He-Ne laser (632 nm, nominal output 10 mW). The laser beam was introduced through an Olympus BX41 microscope and focused on the sample using a 10× objective lens (NA = 0.25). Raman-shift calibration was performed using the 520.7 cm^{-1} band of silicon before each measurement session. Spectra were acquired in confocal mode using a 100 μm confocal hole and a 600 gr/mm grating. Each reported spatial spectrum was obtained from five accumulations of 1 s, yielding a spectral resolution of approximately 2.0 cm^{-1}. Because the numerical aperture of the 10× objective is low, axial sectioning was limited: each spectrum represents a signal integrated over a depth comparable to the cell body rather than an optically isolated plane.

The analyzed spectral windows were approximately 500–3000 cm^{-1} for *C. reinhardtii*, 900–1700 cm^{-1} for *H. pluvialis*, and 400–1800 cm^{-1} for *E. gracilis*. For *C. reinhardtii*, one spectrum was acquired from a single spot (~1.5 μm) near the center of each analyzed cell, and 10 single-cell spectra were analyzed per chamber-height condition.

For *H. pluvialis*, three spatial spectra obtained approximately 4 μm from the cell center were averaged to obtain one spectrum per cell; five cell spectra were then averaged within each chamber. Usable final-day spectra were obtained from four chambers in each of two devices for all three final chamber-height conditions (10, 15, and 40 μm; n = 8 chamber means per condition). Six cells measured in the 40 μm chambers on the loading day provided the reference spectrum shown in Figure 6C.

For *E. gracilis*, one cell with a complete dataset was analyzed per chamber-height condition. For each of these cells, five spectra were acquired at approximately evenly spaced positions along

the longitudinal cell axis, spanning the anterior, anterior-central, central, posterior-central, and posterior cell-body regions. Each cell-level value in Figure 6F is the average of these five spectra. Spectra were baseline-corrected using Origin 9.1 and mean spectra were obtained by arithmetic averaging of the baseline-corrected spectra. No vector, total-area, reference-peak, or other spectral normalization was applied before or after export, so all reported intensities are baseline-corrected detector counts.

Bioproduct-associated responses were evaluated using lipid-associated bands at 1440 and 2900 cm^{-1} for *C. reinhardtii* [29], astaxanthin-associated bands at 1157 and 1516 cm^{-1} for *H. pluvialis* [16, 30], and carotenoid-associated bands at 1159 and 1524 cm^{-1} for *E. gracilis* [31, 32]. For *E. gracilis*, the integral over 400–900 cm^{-1} was used as a polysaccharide-associated regional readout, encompassing reported paramylon-related features near 425 and 893 cm^{-1}; within the 900–1800 cm^{-1} region, which contains ester and carotenoid features, the 1260–1413 cm^{-1} interval was treated as a lipid-associated CH-deformation region that includes the reported ~1296 cm^{-1} CH_2-twist feature [32]. Quantitative comparisons used cell- or chamber-level peak intensities or integrated spectral areas. For the *C. reinhardtii* plots, the reported mean intensities at 1440 and 2900 cm^{-1} correspond to the recorded spectral positions nearest these bands (1440.47 and 2900.55 cm^{-1}, respectively).

Carotenoid band positions vary with effective conjugation length and pigment composition [33]. Band intensities also depend on optical sampling geometry and, for carotenoids, resonance enhancement. The measurements were therefore used for relative comparisons of bioproduct-associated signals rather than absolute intracellular concentrations.

Statistical analysis

Data are presented as mean ± standard error of the mean (SEM) unless otherwise indicated. The sample size and unit used to calculate each summary are specified in the corresponding figure legend. The device was treated as the experimental unit for inference. For *H. pluvialis* and *E. gracilis* cell-number data, chamber values were averaged within each device for each chamber height and chamber heights were compared within devices using repeated-measures ANOVA at each analyzed time point. Inferential comparisons were reported only for these device-level cell-number data. Other readouts were summarized using the means and measures of variability specified in the corresponding figure legends. Statistical significance was defined as $p < 0.05$. Analyses were performed using Python 3.13.5, SciPy 1.17.0, and statsmodels 0.14.6.

Results and Discussion

Platform design and operating principle

The microfluidic platform was designed to impose chamber-height-defined confinement on microalgal cells (Figure 1). The five chamber heights generated species-dependent initial confinement states according to species-specific cell dimensions and morphology (Table 1). The tallest tested chamber served as the designated species-specific control, and shallower chambers imposed progressively stronger confinement. This design allowed all chamber-height conditions for a given species to be screened in parallel on a single chip, and the same chip design to be applied across species with different cell sizes and morphologies.

On-chip cultivation and growth response

On-chip cultivation was first evaluated by monitoring chamber occupancy for *C. reinhardtii* and normalized cell number for *H. pluvialis* and *E. gracilis* (Figure 2). All three species showed increases in chamber occupancy or cell number during cultivation, indicating that the platform

supported microalgal culture while imposing chamber-height-defined confinement. For *C. reinhardtii*, chamber occupancy reports the percentage of analyzable chamber tiles classified as fluorescence-positive, whereas the *H. pluvialis* and *E. gracilis* curves report normalized chamber cell number.

For *C. reinhardtii*, chamber occupancy increased at all tested heights over the 4-day cultivation period. To compare the time course of occupancy buildup across chamber heights, the main plot expresses occupancy relative to the corresponding Day 4 mean for each chamber height, which was defined as 100% (Figure 2A). On the loading day, relative occupancy was approximately 21.8%, 25.7%, 19.3%, and 9.1% of the Day 4 value in the 3, 5, 10, and 15 µm chambers, respectively. By Day 2, these values increased to approximately 86.9%, 99.3%, 95.8%, and 89.7%, indicating that the 5 and 10 µm conditions were closer to their respective Day 4 occupancy values by Day 2 than the 3 and 15 µm conditions. The corresponding raw fluorescence-

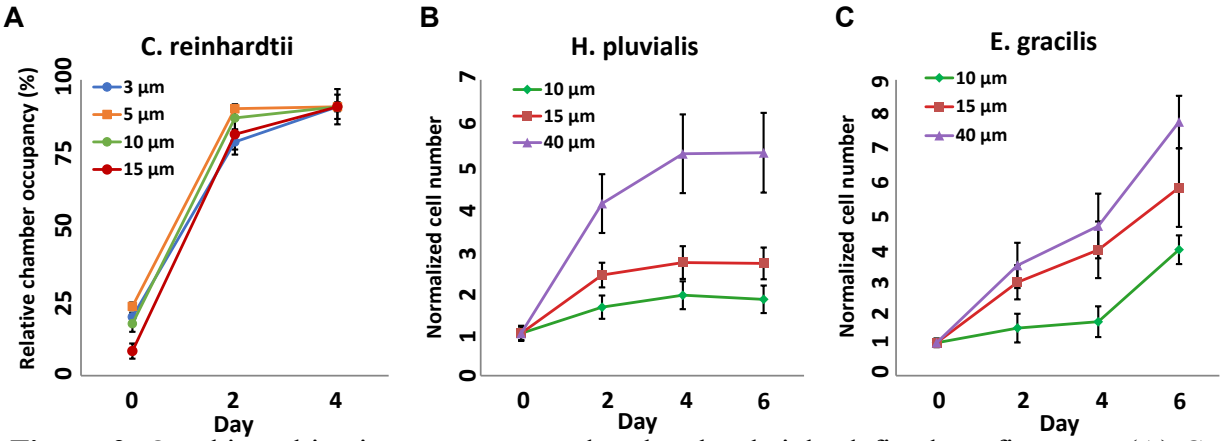

Figure 2. On-chip cultivation responses under chamber-height-defined confinement. (A) C. reinhardtii chamber occupancy in 3, 5, 10, and 15 µm chambers through Day 4, normalized to the Day 4 mean of each condition (100%); mean ± SEM, n = 3 devices (four chambers per height per device). Raw values and representative images are shown in Figure S2. (B) H. pluvialis and (C) E. gracilis cell number normalized to the loading day in 10, 15, and 40 µm chambers. The 40 µm condition is the on-chip control for each species. Data in (B, C) are mean ± SEM of 9, 8, and 12 chambers (10, 15, and 40 µm) for H. pluvialis and 8 chambers per condition for E. gracilis.

positive chamber occupancy values are shown in Figure S2A. In the 5 μm condition, representative Day 4 images showed cells near or beyond the culture-chamber boundary (Figure S2D), as the chamber became densely occupied. The relative values report proximity to the condition-specific Day 4 endpoint.

For *H. pluvialis*, mean normalized cell numbers were lower under confinement than in the 40 μm on-chip control. By Day 6, the chamber-level means shown in Figure 2B reached approximately 1.8-, 2.7-, and 5.3-fold in the 10, 15, and 40 μm chambers, respectively. Repeated-measures ANOVA did not detect a significant chamber-height effect on Day 2, Day 4, or Day 6 ($p = 0.160$, 0.179, and 0.163, respectively).

For *E. gracilis*, cell number increased over 6 days in all tested chambers, with lower mean net cell-number accumulation in shallower chambers. By Day 6, the chamber-level means shown in Figure 2C reached approximately 3.8-, 5.7-, and 7.7-fold in the 10, 15, and 40 μm chambers, respectively. The 10 μm condition gave the lowest mean net cell-number accumulation at all post-loading time points, and the ordering 10 μm < 15 μm < 40 μm was preserved in both devices on Days 2 and 4. Repeated-measures ANOVA did not detect a significant chamber-height effect on Day 2, Day 4, or Day 6 ($p = 0.254$, 0.287, and 0.708, respectively).

Together, these results show that all three species could be cultured on the device, but their observed response patterns differed. *C. reinhardtii* showed rapid chamber occupancy buildup under all tested heights, while the more confined conditions showed lower mean cell-number accumulation in *H. pluvialis* and *E. gracilis*.

Morphological and phenotypic responses

Beyond chamber occupancy and cell number, chamber-height-defined confinement produced species-specific changes in cell morphology and phenotype, which were quantified from daily microscopic images.

For *C. reinhardtii*, projected cell diameter was used to evaluate changes in apparent cell size during cultivation (Figure 3). In the 5 μm chambers, the mean projected diameter increased transiently on Day 1, decreased to approximately 9.2 μm on Day 3, and recovered by Day 4, whereas the 15 μm control varied over a narrower range. The cumulative distributions showed corresponding shifts in individual-cell projected diameter, with a pronounced transient shift toward smaller apparent cell sizes in the 5 μm chambers on Day 3. Overall, confinement altered and shifted the projected cell-size distribution over time, but no monotonic increase or decrease was observed.

For *H. pluvialis*, red-cyst formation was evaluated from representative microscopy images and the red-cyst area fraction (red-pigmented projected area divided by total cell area; Figure 4). No red cysts were detected on the loading day, whereas red-cyst area fractions differed by chamber height and cultivation day; the 40 µm condition, for example, showed a decrease between Days 2

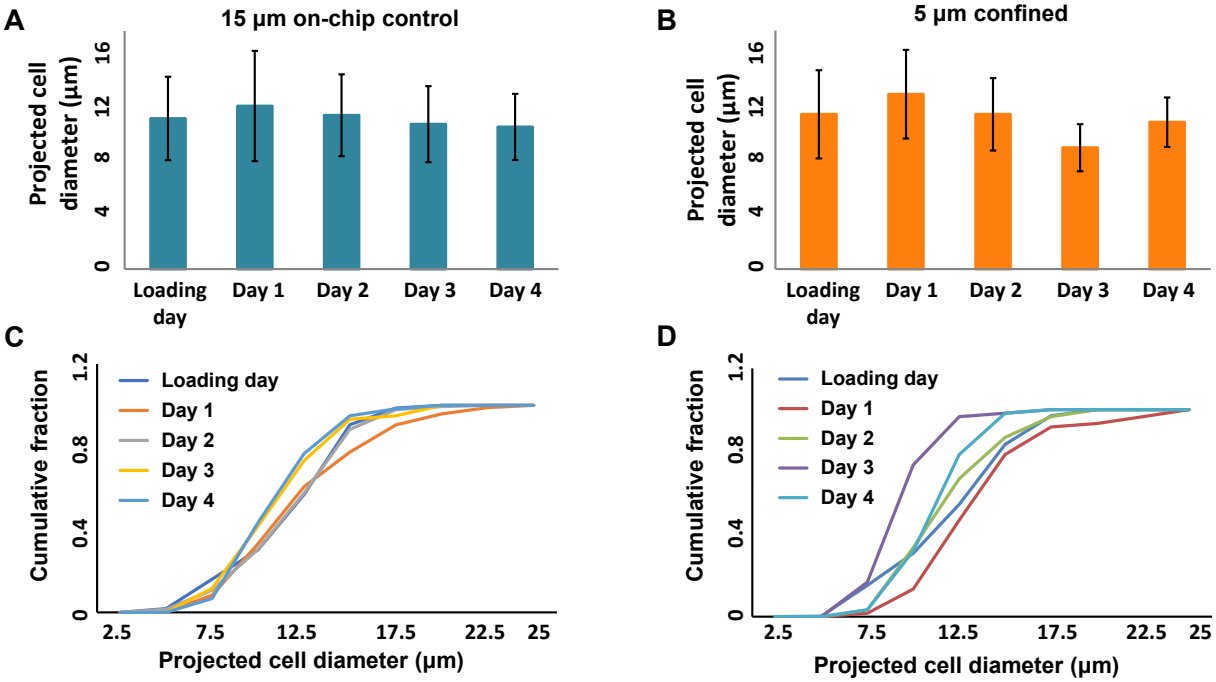

Figure 3. Projected cell-diameter response of C. reinhardtii under chamber-height-defined confinement. (A, C) 15 µm on-chip control; (B, D) 5 µm confined condition. (A, B) Projected two-dimensional diameter from loading through Day 4 (mean ± SD; n = 60–780 cells per condition/time point pooled from three chamber image sets). (C, D) Cumulative distributions of individual-cell projected diameters.

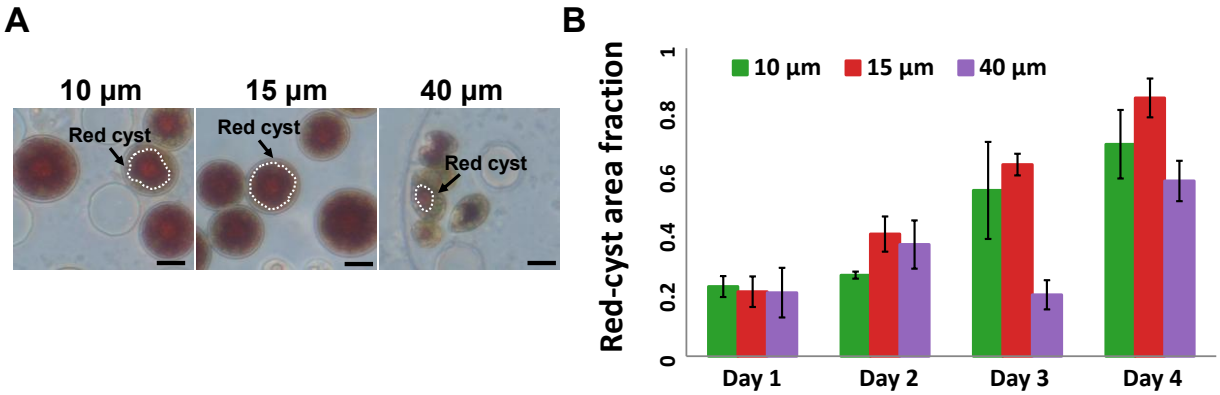

Figure 4. Red-cyst phenotype of *H. pluvialis*. (A) Representative micrographs from 10, 15, and 40 µm chambers (scale bars = 20 µm). (B) Red-cyst area fraction on Days 1-4; mean ± SEM of chamber means (n = 2-3 chambers per condition and day). Loading-day values are omitted because no red cysts were detected, and later days were excluded because cell boundaries could not be segmented reliably.

and 3 before increasing on Day 4. On Day 4, the mean red-cyst area fractions for the 10, 15, and 40 µm conditions were 0.688, 0.838, and 0.569, respectively, with the 15 µm condition showing the highest chamber-mean fraction among the tested conditions. The 40 µm on-chip control also exhibited red-pigmented cells, indicating that encystment proceeded even in the tallest chamber.

For *E. gracilis*, morphology was assessed using a shape index defined as minor axis / major axis, with larger values indicating a more rounded cell shape (Figure 5). The three chamber-height conditions showed similar shape-index values on the loading day, whereas the 10 µm chamber gave the highest mean shape index from Day 2 onward, preserving the ordering 10 µm > 15 µm > 40 µm at later time points. On Day 6, mean projected major and minor axes of cells in the 10 µm chambers were approximately 23.4 and 15.9 µm, compared with loading-day means of 31.6 and 12.6 µm pooled across chamber heights, indicating a more compact projected cell morphology.

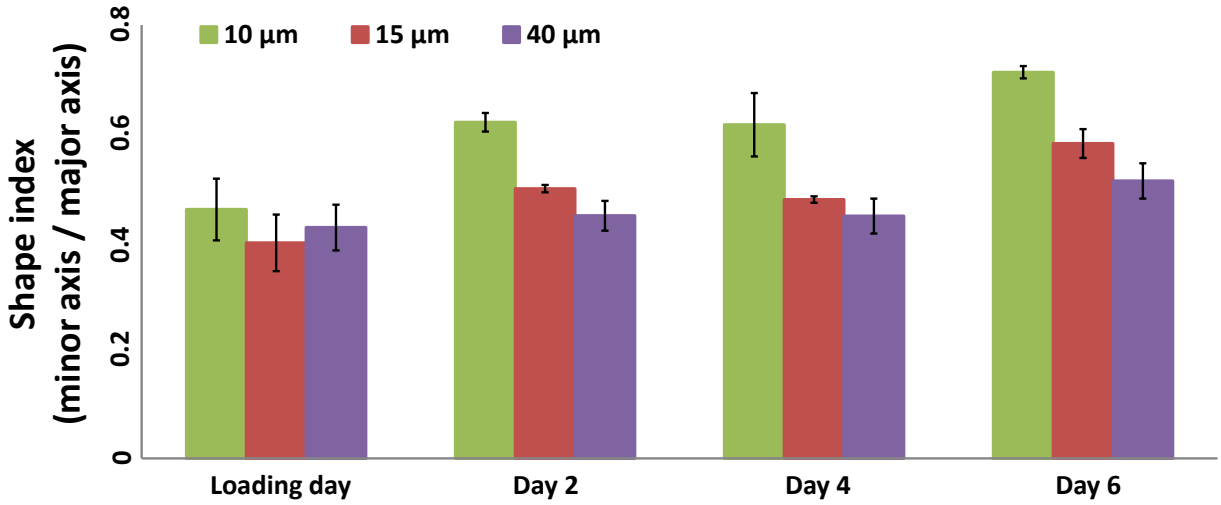

Figure 5. Morphological response of *E. gracilis* under chamber-height-defined confinement. Cells in 10, 15, and 40 µm chambers were evaluated on the loading day and on Days 2, 4, and 6. Shape index = minor axis / major axis; higher values indicate a rounder projected cell shape. Data are mean ± SEM across chamber means (n = 8 per condition).

Raman-based single-cell bioproduct readout

Raman spectroscopy was used to measure bioproduct-associated signals in cells cultured under different chamber-height conditions (Figure 6). Mean spectra were used to compare overall spectral profiles, while peak intensities or integrated areas were used for quantitative comparison.

For *C. reinhardtii*, spectra were acquired on Day 4 from cells cultured in the 3, 5, 10, and 15 µm chambers (Figures 6A and 6B). The spectra contained bands related to lipids (1260, 1440, and 2900 cm^{-1}), carotenoids (1160 and 1530 cm^{-1}), and protein (~1003 cm^{-1}). Both lipid-associated bands selected for quantification, 1440 and 2900 cm^{-1}, reached their highest mean values in confined chambers rather than in the 15 µm control, but peaked at different chamber heights: 1440 cm^{-1} at 5 µm and 2900 cm^{-1} at 3 µm. This band-specific behavior may partly reflect the measurement geometry.

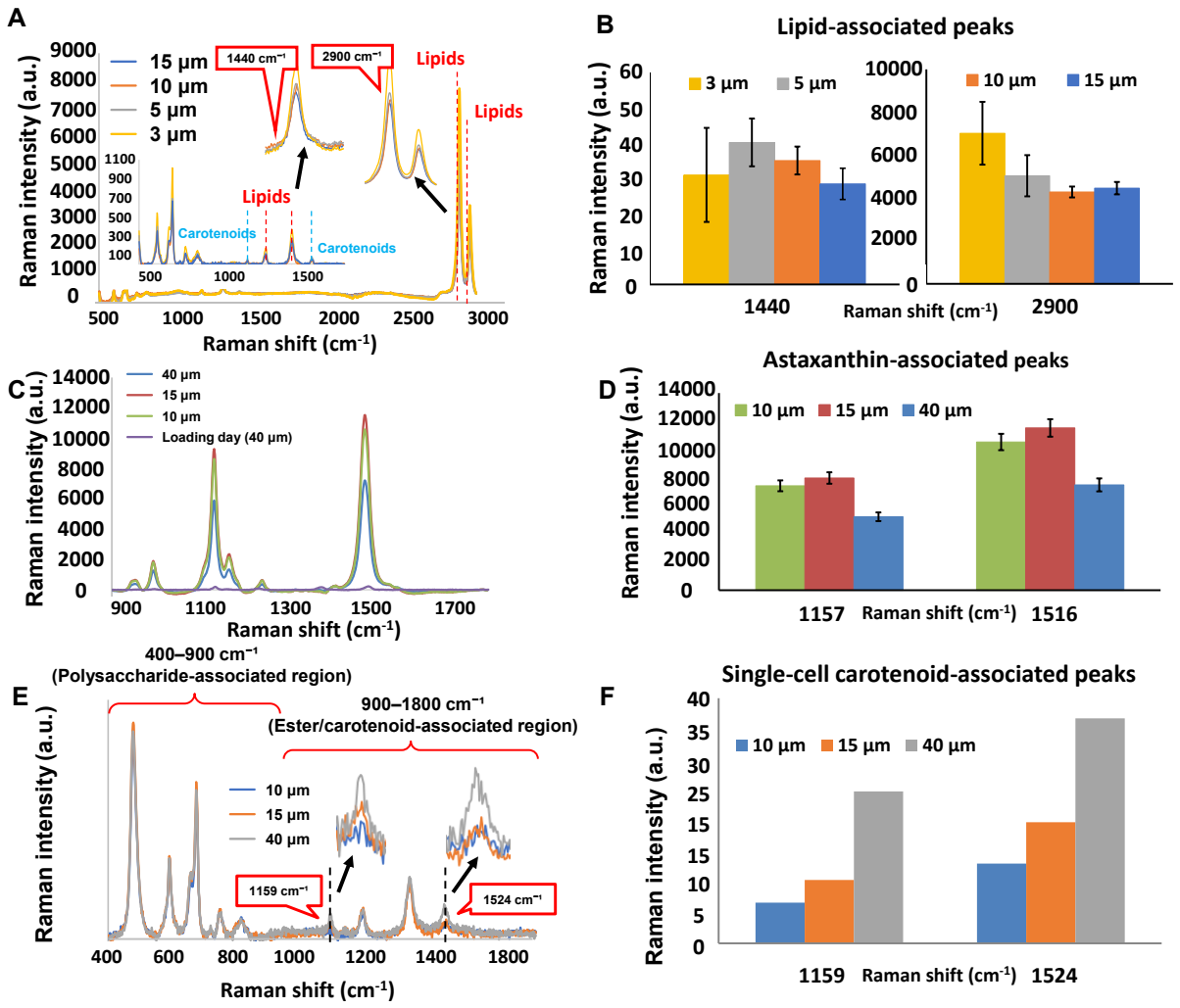

Figure 6. Raman bioproduct-associated readouts under chamber-height-defined confinement. (A, B) *C. reinhardtii*, Day 4: mean spectra and lipid-associated intensities at 1440 and 2900 cm^{-1} (n = 10 cells per condition). (C, D) *H. pluvialis*, Day 6: mean spectra and astaxanthin-associated intensities at 1157 and 1516 cm^{-1}, with the loading-day spectrum from the 40 µm chamber included for comparison (n = 8 chamber means per condition from two devices). (E, F) *E. gracilis*, Day 6: spectra and single-cell carotenoid-associated readouts at 1159 and 1524 cm^{-1} (one cell per condition). Data in (B, D) are shown as mean ± SEM; (F) shows one cell-level mean per condition without error bars.

For *H. pluvialis*, spectra were acquired on Day 6, and the astaxanthin-associated bands at 1157 and 1516 cm^{-1} were used for quantitative comparison (Figures 6C and 6D). The 15 µm chamber showed the highest mean intensity at both bands among the tested on-chip conditions,

consistent with its higher mean red-cyst area fraction and with the favorable ranking of the 15 μm chamber in our previous study [16]. Direct comparison with our previous study is limited by differences in reference conditions and measurement time points. The present study used a 40 μm on-chip control that also showed red-cyst formation and acquired Raman spectra on Day 6 rather than Day 7; the Raman intensity differences should therefore not be directly equated with the earlier fold-change value.

For *E. gracilis*, spectra were acquired on Day 6 from cells in the 10, 15, and 40 μm chambers (Figures 6E and 6F). The integrated polysaccharide-associated region (400–900 cm^{-1}) and lipid-associated region (1260–1413 cm^{-1}) showed no comparable trend among the three conditions. In the cells examined, carotenoid-associated intensities at 1159 and 1524 cm^{-1} were lower in the 10 and 15 μm cells than in the 40 μm cell, with the lowest values in the 10 μm chamber.

Across the three species, the platform detected different bioproduct-associated Raman signal patterns: *C. reinhardtii* showed band-specific lipid-associated responses; *H. pluvialis* showed the highest mean astaxanthin-associated response at 15 μm among the tested on-chip conditions; and the *E. gracilis* cells examined under confinement showed lower carotenoid-associated signals. These patterns indicate that stronger confinement was not uniformly associated with higher signals across the selected Raman readouts. The platform thus enables comparison of chamber-height conditions according to the species and bioproduct-associated readout of interest.

On-chip comparative bioproduct screening

The combined growth, morphology or phenotype, and Raman readouts (Table 2) show that

chamber height functioned as a species- and readout-dependent screening variable rather than as a universal measure of confinement. The same device design was used across species, with species-appropriate subsets of chamber heights. Each species experienced confinement in a different physical context according to its cell size, morphology, and deformability. Thus, the same nominal chamber height did not have the same biological or geometrical meaning for *C. reinhardtii*, *H. pluvialis*, and *E. gracilis*. The comparative results also show that the chamber-height rankings depended on the readout. In *C. reinhardtii*, the two lipid-associated Raman bands reached their highest mean intensities at different chamber heights. In *H. pluvialis*, red-cyst area fraction and astaxanthin-associated Raman readouts were more closely aligned, with the 15 μm chamber ranking highest among the tested on-chip conditions. In *E. gracilis*, shallower chambers were associated with a more compact projected morphology, while the cells examined under confinement showed lower carotenoid-associated Raman signals. These differences highlight the value of combining growth, morphology or phenotype, and Raman readouts rather than relying on

Table 2. Summary of species- and readout-specific responses to chamber-height-defined confinement (Figures 2–6). Entries cover chamber occupancy or cell-number accumulation, morphology/phenotype, and bioproduct-associated Raman responses across the three species. *E. gracilis* Raman data reflect one cell per condition.

Species	Cultivation / growth response	Morphology / phenotype	Bioproduct-associated Raman response	Interpretation
C. reinhardtii	Chamber occupancy increased across all tested heights; by Day 2, the 5 and 10 μm conditions were closer to their respective Day 4 values.	The 5 μm chamber showed a transient shift in the projected cell-size distribution, most clearly on Day 3.	Lipid-associated Raman signals were peak-specific: 1440 cm^{-1} was highest at 5 μm, whereas 2900 cm^{-1} was highest at 3 μm.	Different confinement levels favored different lipid-associated Raman responses; the lipid-band comparison is descriptive and not internally referenced.
H. pluvialis	The 40 μm on-chip control showed the highest mean cell-number accumulation; more confined conditions had lower means.	The 15 μm chamber showed the highest mean red-cyst area fraction among tested conditions.	The 15 μm chamber produced the highest mean astaxanthin-associated signals at both 1157 and 1516 cm^{-1}.	The 15 μm condition further supports the favorable astaxanthin-rich phenotype identified in the previous study.
E. gracilis	Mean cell-number accumulation was numerically lowest in the 10 μm condition at the measured post-loading time points.	The 10 μm chamber produced the strongest increase in shape index, indicating a more rounded cell shape.	Retained single-cell Raman summaries suggested lower carotenoid-associated signals at 10 and 15 μm than at 40 μm.	The mean shape index was highest in the 10 μm condition, while the Raman trend remains preliminary and is based on one traceable cell per height.

a single endpoint.

This cross-species comparison illustrates the main utility of the platform: it can prioritize chamber-height conditions and readouts for further validation while preserving species-specific interpretation. For spherical or approximately spherical cells, chamber height primarily represented vertical compression, whereas for elongated and deformable cells such as *E. gracilis*, geometric restriction and orientation constraints were also important. The platform therefore provides a common experimental format for comparing microalgal responses, while avoiding the assumption that a given chamber height imposes equivalent confinement across different cell types. The species-dependent responses may reflect differences in how mechanical load is transmitted through distinct cell architectures, including the wall-less *C. reinhardtii* cw15 strain, the encysting *H. pluvialis* cells, and the deformable pellicle of *E. gracilis*. Systematic mechanistic studies, such as comparing walled and wall-less strains on the same chip, would be a useful future extension. Raman readouts represent relative, geometry-sensitive spectral signals rather than absolute intracellular concentrations. Future studies should validate Raman-based bioproduct readouts using independent biochemical assays. Overall, the present platform provides a practical framework for comparative microalgal screening and for prioritizing species-specific chamber-height conditions for follow-up studies.

Conclusion

In this study, we developed a star-shaped microfluidic platform that applies chamber-height-defined confinement to microalgal cells and enables the comparison of multiple chamber-height conditions on a chip for each species, using the same device design across species. By integrating multiple chamber heights with on-chip cultivation, image-based phenotypic analysis, and single-

cell Raman readout, the platform allowed growth, morphology or phenotype, and bioproduct-associated Raman signals to be evaluated within a common device format. *C. reinhardtii* showed substantial chamber occupancy across all tested heights, together with chamber-height-dependent changes in projected cell-size distribution and lipid-associated Raman signals, with the two lipid-associated bands reaching their highest mean intensities at different chamber heights. *H. pluvialis* exhibited the highest mean red-cyst area fraction and astaxanthin-associated Raman intensities at 15 μm among the tested on-chip conditions. *E. gracilis* displayed a more compact morphology in shallower chambers, while single-cell Raman measurements showed lower carotenoid-associated signals in the cells examined under confinement. Overall, this platform provides a practical approach for comparative microalgal screening and for prioritizing chamber-height conditions according to the species and readout of interest.

Declaration

Author contributions

J.Y.: conceptualization, methodology, investigation, formal analysis, visualization, writing-original draft. J.Y.K.: supervision, writing-review and editing. H.K.: methodology, writing-review and editing. A.P.: methodology. J.P.: conceptualization, methodology, investigation, supervision, funding acquisition, writing-review and editing. All authors have approved the final version of the manuscript.

Conflicts of interest

There are no conflicts of interest to declare.

Fundings

This work was supported by the NRF grant funded by the Korea government (MSIT) [grant number RS-2025-00562827], Ministry of SMEs and Startups (MSS, Korea) (No. RS-2026-25526379), and by a Korea University Grant.

Acknowledgements

The authors thank the W. M. Keck Center for Cellular Imaging at the University of Virginia for technical support during data acquisition.

References

1. P. Spolaore, C. Joannis-Cassan, E. Duran and A. Isambert, *J. Biosci. Bioeng.*, 2006, **101**, 87–96.
2. M. A. Borowitzka, *J. Appl. Phycol.*, 2013, **25**, 743–756.
3. Z. T. Wang, N. Ullrich, S. Joo, S. Waffenschmidt and U. Goodenough, *Eukaryotic Cell*, 2009, **8**, 1856–1868.
4. M. Guerin, M. E. Huntley and M. Olaizola, *Trends Biotechnol.*, 2003, **21**, 210–216.
5. A. Gissibl, A. Sun, A. Care, H. Nevalainen and A. Sunna, *Front. Bioeng. Biotechnol.*, 2019, **7**, 108.
6. E. C. O'Neill, M. Trick, L. Hill, M. Rejzek, R. G. Dusi, C. J. Hamilton, P. V. Zimba, B. Henrissat and R. A. Field, *Mol. BioSyst.*, 2015, **11**, 2808–2820.
7. T. Watanabe, R. Shimada, A. Matsuyama, M. Yuasa, H. Sawamura, E. Yoshida and K. Suzuki, *Food Funct.*, 2013, **4**, 1685–1690.
8. N. Koizumi, H. Sakagami, A. Utsumi, S. Fujinaga, M. Takeda, K. Asano, I. Sugawara, S. Ichikawa, H. Kondo, S. Mori, K. Miyatake, Y. Nakano, H. Nakashima, T. Murakami, N. Miyano and N. Yamamoto, *Antiviral Res.*, 1993, **21**, 1–14.
9. Z. Chen, Y. Chen, H. Zhang, H. Qin, J. He, Z. Zheng, L. Zhao, A. Lei and J. Wang, *Front. Bioeng. Biotechnol.*, 2022, **10**, 827513.
10. H. Takeyama, A. Kanamaru, Y. Yoshino, H. Kakuta, Y. Kawamura and T. Matsunaga, *Biotechnol. Bioeng.*, 1997, **53**, 185–190.
11. K. K. Sharma, H. Schuhmann and P. M. Schenk, *Energies*, 2012, **5**, 1532–1553.
12. S. Boussiba, *Physiol. Plant.*, 2000, **108**, 111–117.
13. S.-M. Paik, S.-J. Sim and N. L. Jeon, *Bioresour. Technol.*, 2017, **233**, 433–437.

14. M. K. Cho and H. S. Shin, *Sci. Rep.*, 2016, **6**, 32860.
15. S. K. Min, G. H. Yoon, J. H. Joo, S. J. Sim and H. S. Shin, *Sci. Rep.*, 2014, **4**, 4675.
16. J. Yao, H. S. Kim, J. Y. Kim, Y.-E. Choi and J. Park, *Lab Chip*, 2020, **20**, 647–654.
17. G. Noselli, A. Beran, M. Arroyo and A. DeSimone, *Nat. Phys.*, 2019, **15**, 496–502.
18. E. H. Harris, *The Chlamydomonas Sourcebook: Introduction to Chlamydomonas and Its Laboratory Use*, Academic Press, Oxford, 2nd edn, 2009.
19. M. M. R. Shah, Y. Liang, J. J. Cheng and M. Daroch, *Front. Plant Sci.*, 2016, **7**, 531.
20. D. R. Davies and A. Plaskitt, *Genet. Res.*, 1971, **17**, 33–43.
21. D. S. Gorman and R. P. Levine, *Proc. Natl. Acad. Sci. U. S. A.*, 1965, **54**, 1665–1669.
22. J. Fábregas, A. Domínguez, M. Regueiro, A. Maseda and A. Otero, *Appl. Microbiol. Biotechnol.*, 2000, **53**, 530–535.
23. M. Wayama, S. Ota, H. Matsuura, N. Nango, A. Hirata and S. Kawano, *PLoS One*, 2013, **8**, e53618.
24. V. Zimorski, C. Rauch, J. J. van Hellemond, A. G. M. Tielens and W. F. Martin, *Adv. Exp. Med. Biol.*, 2017, **979**, 19–37.
25. W. Xie, X. Li, H. Xu, F. Chen, K.-W. Cheng, H. Liu and B. Liu, *Mar. Drugs*, 2023, **21**, 519.
26. M. T. Hasan, A. Sun, B. Khatiwada, L. McQuade, M. Mirzaei, J. Teo, G. Hobba, A. Sunna and H. Nevalainen, *Algal Res.*, 2019, **43**, 101638.
27. L. E. Koren and S. H. Hutner, *J. Protozool.*, 1967, **14**(Suppl.), 17 (abstract).
28. J. Schindelin, I. Arganda-Carreras, E. Frise, V. Kaynig, M. Longair, T. Pietzsch, S. Preibisch, C. Rueden, S. Saalfeld, B. Schmid, J.-Y. Tinevez, D. J. White, V. Hartenstein, K. Eliceiri, P. Tomancak and A. Cardona, *Nat. Methods*, 2012, **9**, 676–682.

29. H. Wu, J. V. Volponi, A. E. Oliver, A. N. Parikh, B. A. Simmons and S. Singh, *Proc. Natl. Acad. Sci. U. S. A.*, 2011, **108**, 3809–3814.

30. A. Kaczor, K. Turnau and M. Baranska, *Analyst*, 2011, **136**, 1109–1112.

31. Y. Kubo, T. Ikeda, S.-Y. Yang and M. Tsuboi, *Appl. Spectrosc.*, 2000, **54**, 1114–1119.

32. K. Iwasaki, A. Kaneko, Y. Tanaka, T. Ishikawa, H. Noothalapati and T. Yamamoto, *Biotechnol. Biofuels*, 2019, **12**, 128.

33. R. Withnall, B. Z. Chowdhry, J. Silver, H. G. M. Edwards and L. F. C. de Oliveira, *Spectrochim. Acta, Part A*, 2003, **59**, 2207–2212.

Supplementary Files

This is a list of supplementary files associated with this preprint. Click to download.

- Supplements20261109final.docx